Title

Estimated global ocean wind power potential from QuikSCAT observations, accounting for turbine characteristics and siting

Journal

Journal of Geophysical Research, 115(D9)

ISSN

0148-0227

Authors

Capps, Scott B
Zender, Charles S

Publication Date

2010-05-05

DOI

10.1029/2009JD012679

JOURNAL OF GEOPHYSICAL RESEARCH, VOL. 115, D09101, doi:10.1029/2009JD012679, 2010

Estimated global ocean wind power potential from QuikSCAT observations, accounting for turbine characteristics and siting

Scott B. Capps[1] and Charles S. Zender[1]

Received 17 June 2009; revised 13 November 2009; accepted 1 December 2009; published 5 May 2010.

[1] For the first time, global ocean usable wind power is evaluated for modern offshore turbine characteristics including hub height, usable portion of the wind speed distribution, and siting depth. Mean wind power increases by 30%, 69%, and 73% within the tropics and Northern and Southern Hemisphere extratropics, respectively, between hub heights of 10 m and 100 m. A turbine with a cut-out speed of 25 m s^{-1} (30 m s^{-1}) within the Northern Hemisphere storm track harvests between 55% (82%) and 85% (>98%) of available power. Within this region, a 2–3 m s^{-1} change in cut-out speed can result in a 5–7% change in usable power. Eighty meter wind power accumulates at a rate of 20–45 MW km^2 m^{-2} per meter depth increase from the shore to the shelf break. Beyond the shelf break, wind power accumulates at a slower rate (<12 MW km^2 m^{-2} m^{-1}). The combined impact of all three characteristics on available wind power is assessed for three technology tiers: existing, planned, and future innovations. Usable percent of 80 m available global ocean wind power ranges from 0.40% for existing to 2.73% for future envisioned turbine specifications. Offshore wind power production is estimated using three offshore wind turbine power curves, three ocean depth limits and two siting densities. Global offshore wind power is as much as 39 TW (54% of onshore) and is maximized for the smallest and least powerful of the three turbine specifications evaluated.

Citation: Capps, S. B., and C. S. Zender (2010), Estimated global ocean wind power potential from QuikSCAT observations, accounting for turbine characteristics and siting, *J. Geophys. Res.*, *115*, D09101, doi:10.1029/2009JD012679.

1. Introduction

[2] New, renewable energy sources are important for human and wildlife health, energy security and mitigating climate change. Wind power ranks at the top of alternative energy sources as a solution to global warming [*Jacobson*, 2009]. Available global ocean wind power at the height of a typical modern wind turbine (80 m) has been assessed [*Capps and Zender*, 2009]. Turbine hub heights vary across manufacturers and models. Heights higher than 80 m typically capture more power while lower heights capture less. Further, wind turbines only operate over a certain range of wind speeds (usable speeds) capturing a portion of this available power. Deeper continental shelf waters provide more siting space and power but, at a higher cost. The depth at which the benefit of added power exceeds the cost will continue to deepen with technological advances. Thus, we extend the work of *Capps and Zender* [2009], providing a global ocean wind power assessment applicable to multiple offshore wind turbine specifications including hub height, usable wind speeds and siting depth.

[3] Wind energy continues to achieve record growth, doubling in global capacity from 2005 to 2008 [*American Wind Energy Association*, 2009]. Life cycle assessments of modern-day wind turbines confirm the environmental benefit of wind farms [*Martinez et al.*, 2009], unmatched by other clean energy sources [*Jacobson*, 2009]. Onshore wind power costs are currently competitive with conventional electricity sources. In contrast, offshore wind energy is currently 1.5–2.0 times more expensive than onshore [*Snyder and Kaiser*, 2009; *Breton and Moe*, 2009]. However, onshore power has foreseeable limitations which could make offshore power more competitive. For example, the land surface (13% of global land) with economically viable wind power is quickly being filled [*Breton and Moe*, 2009]. Of the contiguous United States, 28 have a coastal border and consume 78% of U.S. electricity (State electricity sales spreadsheet, Energy Information Administration, http://www.eia.doe.gov). Yet, only 6 of these 28 states have enough onshore wind resources to meet more than 20% of their electricity requirements [*Department of Energy* (*DOE*), 2008]. In contrast, *Kempton et al.* [2007] estimated offshore wind energy suitable to exceed the demand of several nearby coastal border states. Also, offshore turbine size is not constrained due to the relative ease and reduced cost of transporting larger turbines over water compared to land. Further, future technological achievements and learning should reduce the costs of offshore wind power while overcoming navigational safety issues and reducing the impact on marine mammals [*Snyder and Kaiser*, 2009]. For example, lighter weight generators with double the power are currently being developed and, if

[1]Department of Earth System Science, University of California, Irvine, California, USA.

0148-0227/10/2009JD012679

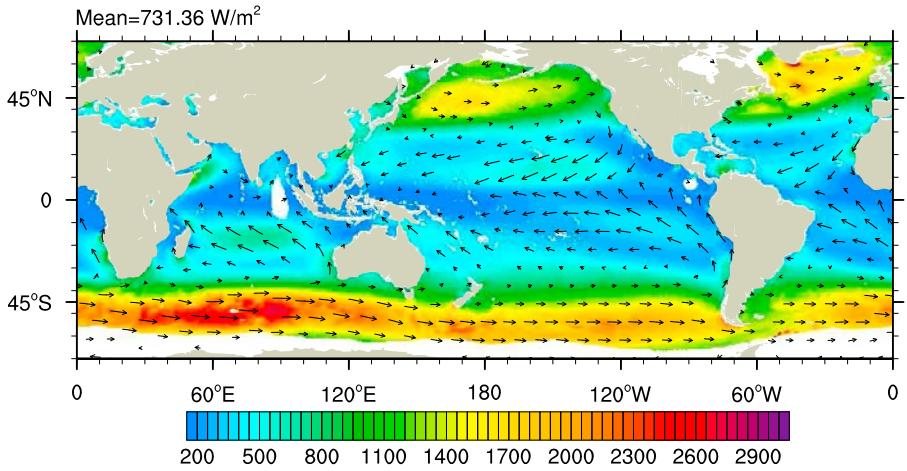

Figure 1. The 2000–2006 80 m wind power density (W m^{-2}).

successful, could reduce offshore wind power costs tremendously [*Matthews*, 2009].

[4] Europe currently has more than 30 offshore wind farms in operation or construction while North American offshore farms are in the planning stages [*Breton and Moe*, 2009]. Offshore winds are typically stronger and more persistent than onshore [*Pryor and Barthelmie*, 2002], providing as much as 150% more electricity and reducing turbine fatigue [*Snyder and Kaiser*, 2009]. With respect to typical land turbines, offshore turbines can be closer to densely populated coasts of continents but, far enough offshore to be inaudible and invisible. Placed far enough away to be unheard, offshore wind farms can contain larger, more powerful turbines. Finally, a benefit of offshore wind beyond that of increased wind resources could be the mitigation of climate change [*Salter et al.*, 2008].

[5] *Capps and Zender* [2009] evaluated global ocean 80 m wind power accounting for surface layer stability. In this study, most of our analysis is at 80 m, the height of typical modern-day turbines and other studies [*Pimenta et al.*, 2008; *Archer and Jacobson*, 2005]. Available 2000–2006 80 m wind power densities between 100 and 500 W m^{-2} exist over approximately 50% of the ice-free ocean surface area (Figure 1). Regions with these relatively low-to-moderate wind power densities include the horse latitudes, trade wind regions and intertropical convergence zone. In contrast, high wind power (>1000 W m^{-2}) regions cover 25% of the ice-free ocean and include the storm tracks, tip jet and gap wind regions.

[6] We extrapolate near-surface winds to multiple heights up through 100 m using thermodynamic data and methods described in sections 2 and 3. The sensitivity of wind power to height is then evaluated for multiple regions in section 4.1. Usable power as a fraction of available power is quantified for typical turbine cut-in and cut-out speeds over the global oceans in section 4.2. Section 4.3 examines the relationship between available wind power and siting depth over the continental shelves. Within section 5, we provide an estimate of usable offshore wind power for three wind turbine technology scenarios. Section 5 concludes with a global offshore wind power estimate using three wind turbine power curves, three ocean depth limits and two wind farm siting densities.

2. Data

[7] Without collocated atmospheric sounding observations, vertical wind speed profile estimation given 10 m neutral-stability wind speeds requires surface layer thermodynamic measurements including surface sensible (H_0) heat flux, 2 m air temperature (T_a) and 2 m specific humidity (q_a).

2.1. SeaWinds on QuikSCAT

[8] We use the 7 year (January 2000 through December 2006) level 3 reprocessed 0.25° × 0.25° QuikSCAT 10 m wind speed data set available from the Physical Oceanography Data Active Archive Center. QuikSCAT uses an empirical algorithm to relate backscatter generated by capillary waves to surface stress. 10 m surface winds (~0600 and 1800 local time) are inferred from these stress measurements by assuming a neutrally stable atmosphere [*Liu*, 2002; *Liu et al.*, 2008]. This assumption introduces a bias during nonneutral conditions [*Hoffman and Leidner*, 2005]. Ten meter anemometer winds are typically 0.2 m s^{-1} slower than in situ 10 m neutral-stability winds [*Mears et al.*, 2001; *Chelton and Freilich*, 2005]. Ice- and land-free wind vector cells between 70°N and 70°S (including large inland bodies of water) containing more than 50% of the time series without the possibility of contamination due to rain are evaluated.

[9] There are intrinsic differences between scatterometry-derived winds and those experienced by a wind turbine. The scatterometer 10 m neutral-stability wind speed is relative to the underlying ocean current. In contrast, a wind turbine captures wind at a fixed location. Thus, fast surface ocean currents can cause differences up to 1 m s^{-1} between QuikSCAT wind speeds and those relative to a fixed location [*Kelly et al.*, 2001; *Chelton and Freilich*, 2005]. *Kelly et al.* [2001] found differences between QuikSCAT and buoys of 0.5 m s^{-1} over the slower tropical Pacific equatorial currents. Differences on the order of 1 m s^{-1} can equate to substantial wind power differences. These differences are maximized near the power curve inflection point where as much as 500 kW more (less) power is generated from a 1 m s^{-1}

Table 1. Offshore Megawatt Wind Turbine Specifications

Turbine	Rated Capacity (kW)	Hub Heights (m)	Cut-In and Cut-Out Speeds ($m\ s^{-1}$)
RE Power 5M	5000	90–100	3.5–30.0
GE 3.6 MW	3600	site dependent	3.5–27.0
Vestas V90	3000	80, 105	4.0–25.0

increase (decrease) in wind speed (using a GE3.6sl power curve). However, at speeds between the rated and cut-out speeds, QuikSCAT versus turbine wind speed differences result in no power differences as the power curve asymptotes to the rated power until the cut-out speed. When evaluating the average wind power over a length of time, these potentially positive and negative power differences could offset each other. Further, ocean currents closer to the coast tend to be slower than open ocean currents, thus minimizing scatterometer versus fixed-location wind speed differences in regions evaluated within this study.

2.2. Objectively Analyzed Air-Sea Fluxes

[10] Surface layer thermodynamic data is provided by the Woods Hole Oceanographic Institution third version of global ocean-surface heat flux products released by the Objectively Analyzed air-sea Heat Fluxes (OAFLUX) project [*Yu et al.*, 2008]. Bulk aerodynamic formula physical variables originate from a blend of reanalysis data and satellite measurements. These variables are improved through the use of a variational objective analysis technique. Errors for each variable are estimated using in situ measurements including moored buoys and ship observations. OAFLUX surface energy fluxes are computed using the TOGA COARE bulk flux algorithm 3.0 [*Fairall et al.*, 2003]. We bilinearly interpolate daily OAFLUX H_0, T_a and q_a from 1.0° × 1.0° to match QuikSCAT spatial resolution.

2.3. NCEP-DOE AMIP-II Reanalysis

[11] NCEP-DOE AMIP-II reanalysis data were provided by the NOAA/OAR/ESRL PSD, Boulder, Colorado, USA (http://www.cdc.noaa.gov/) [*Kanamitsu et al.*, 2002]. NCEPII 2.5° × 2.5° daily mean sea level pressure (MSLP) used to calculate air density is regridded to QuikSCAT spatial resolution. NCEPII H and q_a are regridded from T62 to QuikSCAT spatial resolution and are substituted where OAFLUX data are missing.

2.4. Ocean Bathymetry

[12] Ocean depths reported in this study are from NOAA's National Geophysical Data Center global ocean bathymetry and relief data set [*Amante and Eakins*, 2008]. Bathymetry is used to evaluate wind power as a function of siting depth in coastal regions. The one arc-minute resolution bathymetry was regridded to QuikSCAT resolution using local area averaging.

3. Methods

3.1. Wind Speed Extrapolation

[13] The no-slip boundary condition at the surface and ensuing downward momentum transfer result in a typical atmospheric boundary layer (ABL) semilogarithmic wind speed profile. We extrapolate 10 m QuikSCAT winds to multiple levels as high as 100 m. Previous ocean-based regional wind studies use a power-law profile to extrapolate near-surface wind measurements aloft [e.g., *Lu et al.*, 2002], while others use location-specific fitted curves [*Archer and Jacobson*, 2005] or a logarithmic wind profile [e.g., *Pimenta et al.*, 2008]. We apply Monin-Obukhov Similarity Theory (MOST) to account for deviations to the logarithmic wind profile due to thermal stratification (For details, see *Capps and Zender* [2009]). Both the power-law and logarithmic profile do not account for changes in vertical wind shear with respect to surface layer stability. Wind speeds extrapolated vertically using a logarithmic or power-law profile are generally faster (slower) than measured winds within an unstable (stable) surface layer. Large differences (~20–40%) between measured 40 and 80 m winds and those extrapolated vertically from 10 m using the logarithmic profile assumption are significantly reduced while employing MOST [*Lange and Focken*, 2005]. *Lange et al.* [2004] demonstrate the accuracy of MOST at estimating wind shear profiles in an offshore tower environment.

[14] MOST applies within the constant flux surface layer typically found within the lowest 5–10% of the ABL [*Arya*, 2001]. Thus, winds extrapolated to heights greater than the surface layer could have considerable inaccuracies. Over land, the ABL layer height has a large diurnal cycle. For an onshore location, MOST profile correction has been found to fail near 140 m possibly because this height is above the shallow nighttime stable ABL surface layer [*Lange and Focken*, 2005]. The maritime ABL, however, experiences relatively small diurnal height fluctuations with mean stratocumulus-topped maritime ABL heights of 1 km [*Serpetzoglou et al.*, 2008; *Medeiros et al.*, 2004]. Without the availability of accurate global ocean ABL and surface layer height data, we assume heights below 100 m are within the surface layer. The use of surface flux based ABL height diagnostics and/or assimilation of other data sets including upper-level winds could provide wind speed estimates at higher levels and is beyond the scope of this study. In close proximity to the coast, regions of upwelling and eddies can often contribute to finer spatial-scale features not resolved within the OAFLUX data set. The existence of unresolved finer spatial-scale surface fluxes within the 1.0° × 1.0° OAFLUX data set could create differences between vertically extrapolated (from 10 m) and actual wind speeds.

3.2. Truncated Wind Power Density

[15] Usable speed ranges evaluated here are based on three modern turbines suitable for offshore placement: the RE Power Systems 5.0 Megawatt (MW), General Electric 3.6 MW and Vestas V90 3.0 MW turbines (Table 1). We calculate usable wind power density using both discrete QuikSCAT measurements and a truncated wind speed probability density function (PDF). The power density for a cut-in speed of u_1 and cut-out speed of u_2 of a discrete wind speed time series is

$$P_{u_1,u_2}/A_r = \frac{1}{2N}\sum_{i=1}^{n}\rho_i u_i^3, \quad (1)$$

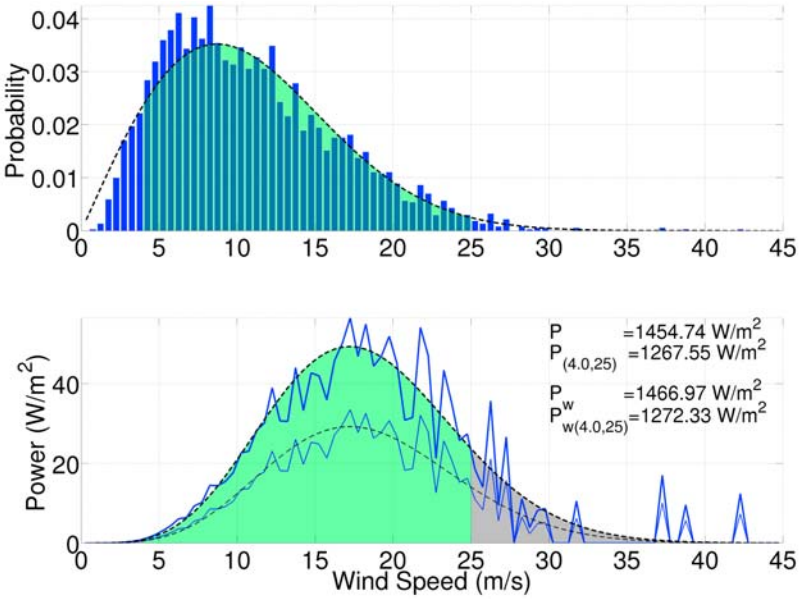

Figure 2. (top) Histogram and fitted Weibull PDF of 2000–2006 80 m winds for a location off the northern California coast (41.625°N latitude, 124.875°W longitude, 0.5 m s^{-1}, bin widths). (bottom) Power density from fitted Weibull (P_w, thick dashed line) and discrete QuikSCAT measurements (P, thick solid line) with Betz Limit power (thin lines).

where A_r is the area swept by the rotors and N and n are the number of observations per grid cell and the number of wind speeds between u_1 and u_2, respectively. Air density (ρ) is calculated daily and is extrapolated vertically using the U.S. standard atmosphere profile.

[16] Following *Capps and Zender* [2009], we fit a two-parameter Weibull PDF to the QuikSCAT time series at each grid cell. Usable wind power density is proportional to the third moment of the truncated Weibull PDF

$$P_w(u_1,u_2)/A_r = \frac{1}{2}\rho c^3\left[\gamma\left(1+\frac{3}{k},\left(\frac{u_2}{c}\right)^k\right)-\gamma\left(1+\frac{3}{k},\left(\frac{u_1}{c}\right)^k\right)\right], \quad (2)$$

where k is the shape parameter, c is the scale parameter, u_1 and u_2 are the cut-in and cut-out speeds, respectively, and γ is the lower incomplete gamma function

$$\gamma(\alpha,x_i) = \int_0^{x_i} t^{\alpha-1}e^{-t}dt, \quad (3)$$

where $\alpha = (1+\frac{3}{k})$ and $x_i = (\frac{u_i}{c})^k$. Surface air density is assumed to be constant (ρ = 1.225 kg m^{-3}) and is extrapolated vertically.

[17] The cubic dependence of wind power upon speed dictates that the bulk of the power comes from wind speeds faster than the mean. Thus, the percent of available power extracted is sensitive to the cut-out speed and is reduced for locations with fast and variable wind speeds. Figure 2 depicts a histogram from QuikSCAT measurements, a fitted Weibull PDF and wind power density curves for coastal waters of northern California. Despite discrepancies, the wind power density from both discrete and fitted distributions are within 1% of each other. Due to fast and variable winds (2000–2006 80m $\overline{U}$ = 10.84 m s^{-1}, σ = 5.68 m s^{-1}), a portion of the positively skewed distribution lies to the right of 25 m s^{-1}. The power density peaks far to the right of the mean with 87% and 13% of power residing to the right of $\overline{U}$ and the 25 m s^{-1} cut-out speed (region shaded in grey), respectively. Per the Betz Limit [*Betz*, 1920], as much as 750 W m^{-2} (59.3%) of the roughly 1270 W m^{-2} from the truncated PDF is extractable.

4. Results

4.1. Global Ocean Wind Power Versus Height

[18] We calculate wind power at multiple heights between 10 m and 100 m to evaluate the sensitivity of wind power to height. At a height z within the surface layer, vertical wind shear is proportional to u_* and an empirically derived similarity function $\phi(\zeta)$ which corrects for stability [*Arya*, 2001],

$$\frac{\partial U}{\partial z} = \frac{u_*}{zk}\phi_m\left(\frac{z}{L}\right). \quad (4)$$

For a given surface layer stability, u_* increases with wind speed, reducing the stability correction ϕ_m (L is proportional to u_*^3). Turbulence becomes more localized (mechanical) and the influence of static stability on the wind speed profile is reduced, increasing vertical wind shear. Also, the cubic dependence of wind power on wind speed results in a greater increase in power per unit increase in wind speed at higher speeds. Thus, regions characterized with frequent high wind speed occurrences [*Capps and Zender*, 2008; *Sampe and Xie*, 2007] gain the most power with increases in turbine hub height.

[19] The 2000–2006 global mean wind power is 60% higher at 100 m (776 W m^{-2}) compared to 10 m (487 W m^{-2}, Figure 3). Rates of increase are typically 2–3 W m^{-2} m^{-1} but, range from 2 W m^{-2} m^{-1} (80 to 100 m) to 5 W m^{-2} m^{-1} (20 to 35 m). Climatological mean and 90th percentile extratropical 10 m winds are much faster (10–12 m s^{-1} and 14–16 m s^{-1},

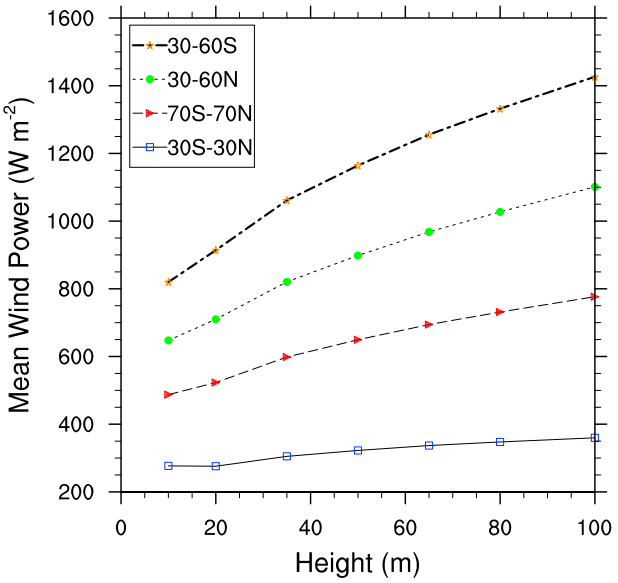

Figure 3. The 2000–2006 mean wind power versus height for four zonal regions (30°S–30°N, 30°S–60°S, 30°N–60°N, and 70°S–70°N) and seven heights (10, 20, 35, 50, 65, 80, and 100 m).

respectively) compared to the tropics (6–8 m s^{-1} and 8–10 m s^{-1}, respectively) [*Monahan*, 2006; *Capps and Zender*, 2008]. Slower winds and nearly logarithmic profiles [*Capps and Zender*, 2009] within the tropics reduce the power gain per height. Mean wind power within the tropics increases by approximately 30% between 10 and 100 m. In comparison, extratropical regions exhibit a larger increase in annual mean wind power with height (Figure 3). Rising from 10 to 100 m, 2000–2006 mean wind power increases by 69% and 73% within the Northern and Southern Hemisphere extratropics, respectively.

[20] The Northern Hemisphere (NH) storm track (ST) has greater interseasonal variability in wind speed statistics (Figure 4) and power [*Capps and Zender*, 2009] compared to the Southern Hemisphere (SH). The NH winter ST has fast 2000–2006 90th percentile 10 m winds (20 m s^{-1}, not shown). DJF 100 m NH ST wind power is approximately 350–550 W m^{-2} greater than 50 m power. This equates to a 7–11 W m^{-2} m^{-1} rate of increase (Figure 5). However, JJA 90th percentile 10 m winds are slower (10 m s^{-1}) due to a relaxed meridional temperature gradient and predominantly stable surface layer. Fast wind regions are typically characterized with larger vertical shear and smaller interstability shear differences. Thus, vertical wind shear in fast wind and unstable surface layers can exceed that in slow wind and slightly stable surface layers. One such region where this occurs is within the NH ST, especially over the North Atlantic Ocean. A substantial decrease in vertical wind shear from NH winter to summer is only partially recovered from an increase in surface layer stability. Thus, JJA NH ST power increase per meter ascent (4–8 W m^{-2} m^{-1}) is lower compared to DJF with the exception of the extremely stable surface layer over the eastern North American continental shelf (12–16 W m^{-2} m^{-1}). In contrast, the SH belt of frequent fast winds [*Sampe and Xie*, 2007] experiences more interseasonally persistent high speed winds (90th percentile 10 m winds between 15 m s^{-1} (DJF) and 19 m s^{-1} (JJA)). JJA power increase is between 6 to 12 W m^{-2} m^{-1} across most of the SH ST while DJF is slightly lower (6–10 W m^{-2} m^{-1}). A stable surface layer near the Kerguelen Plateau during DJF is collocated with large power per height increases (12–14 W m^{-2} m^{-1}, Figure 5).

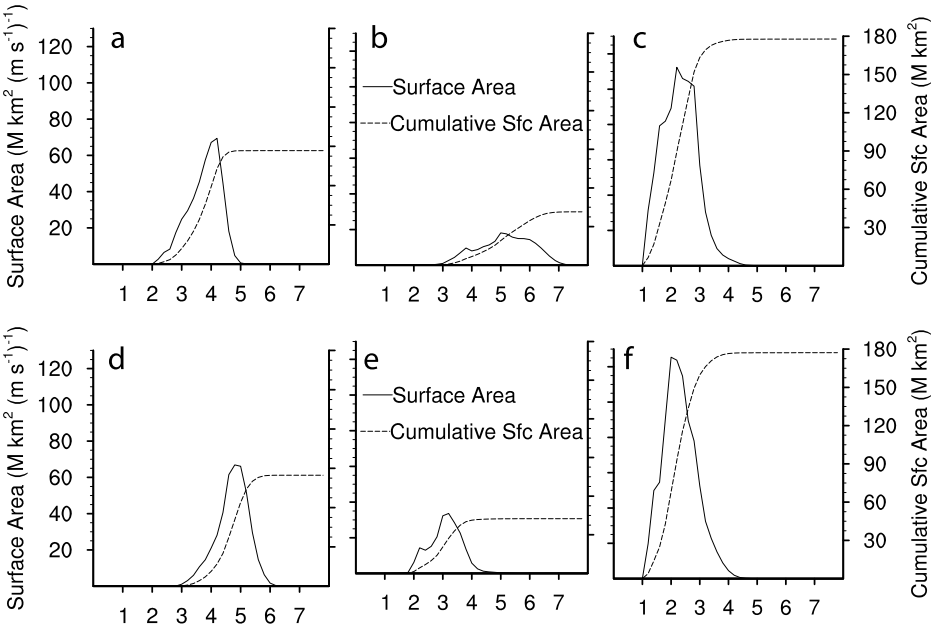

Figure 4. The 2000–2006 (a, b, c) December–January–February (DJF) and (d, e, f) June–July–August (JJA) surface area per unit 80 m wind speed standard deviation and cumulative surface area for three regions: 30°S–60°S (Figures 4a and 4d), 30°N–60°N (Figures 4b and 4e), and 30°S–30°N (Figures 4c and 4f).

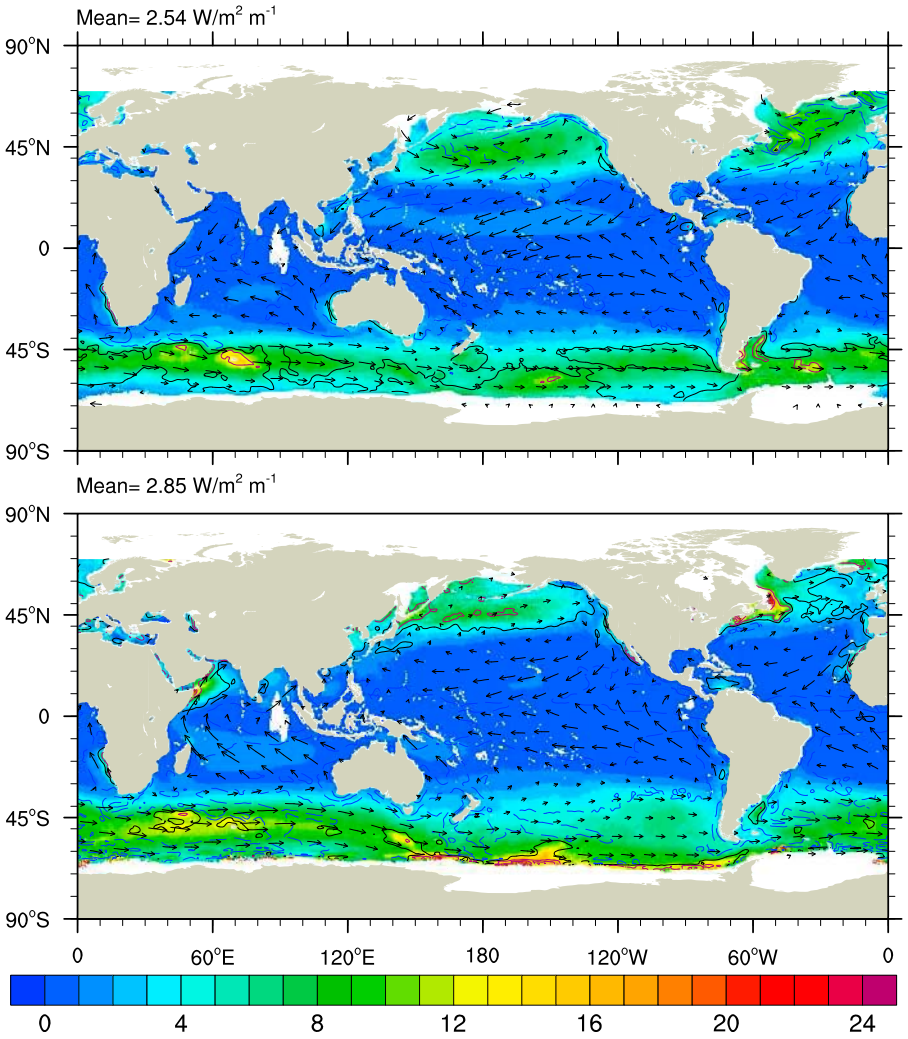

Figure 5. The 2000–2006 mean (top) DJF and (bottom) JJA wind power gain per height (W m^{-2} m^{-1}) between 50 m and 100 m. The 10 m wind vectors with positive (magenta), negative (blue), and zero (black) T_a minus SST contours are shown.

4.2. Usable Power

[21] Usable power, the power harvested between the cut-in and cut-out wind speeds, is dependent upon turbine design and the wind speed distribution. Most modern turbine cut-in speeds range from 3 to 4 m s^{-1}. Wind power is insensitive to this 1 m s^{-1} range in cut-in speed. In contrast, usable power in fast-wind regions may be substantially less depending on the turbine cut-out speed, wind speed PDF center of mass and breadth. We examine ocean regions where wind power is sensitive to the cut-out speeds of modern turbines. The wind power density calculated from fitted Weibull PDFs is truncated between cut-in and cut-out wind speeds of three offshore wind turbines (Table 1). The 2000–2006 80 m global mean available wind power is reduced from 731 W m^{-2} (Figure 1) to 728 W m^{-2}, 720 W m^{-2} and 706 W m^{-2} for usable speed ranges of 3.5–30, 3.5–27 and 4–25 m s^{-1}, respectively.

[22] Wind speed variability typically increases with the mean speed, increasing the likelihood of the wind speed distribution's upper tail to exceed the cut-out speed. Thus, usable power percent of full PDF power declines as winds become more variable (Figure 6). For the three usable speed ranges evaluated, usable power percent of full PDF power begins to drop for standard deviations > 4.0 m s^{-1}. In highly variable regions, ($\sigma > 6.0$ m s^{-1}), usable percent of full power falls below 95, 90 and 80% for usable ranges of 3.5–30, 3.5–27 and 4–25 m s^{-1}, respectively. Fast and variable ($\sigma >$ 6.0 m s^{-1}) NH winter ST winds vanish during NH summer and are seen only in limited locations within the SH winter ST (Figure 4b). Hence, the JJA curve in Figure 6 becomes jagged for $\sigma > 6.4$ m s^{-1}.

[23] Strong ($\overline{U}$ = 11–15 m s^{-1}), variable (σ = 4–7 m s^{-1}) 80 m winter NH ST winds occupy 11% of the global ice-free ocean surface area. Here, a turbine with a cut-out speed of 25 m s^{-1} only harvests between 55 and 85% of available power (Figure 7, left). Collocated with σ maxima (6–7 m s^{-1}) are usable power minima within the winter NH ST. Within these regions, a 2–3 m s^{-1} change in cut-out speed can result in a 5–7% change in usable power (Figure 8). In comparison, wintertime SH circumpolar region σ and $\overline{U}$ range from

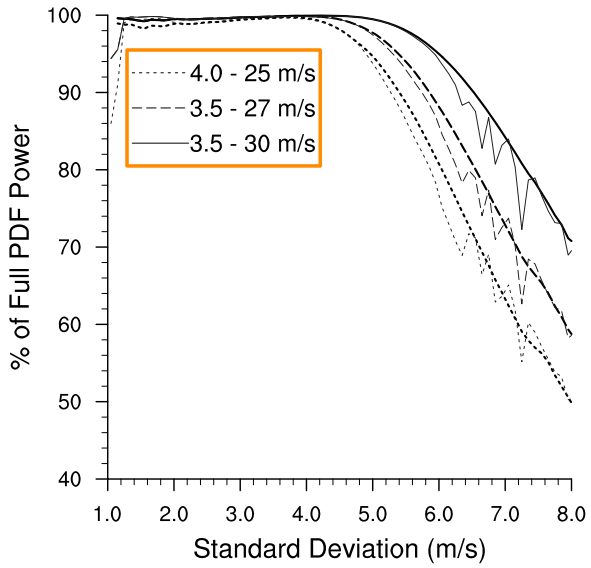

Figure 6. The 2000–2006 DJF (thick black contour) and JJA (thin gray contour) 80 m wind speed standard deviation and bin-averaged usable wind power percent of full PDF power for three usable wind speed ranges (between 70°S and 70°N).

4–6 m s^{-1} and 8–16 m s^{-1}, respectively, occupying more space compared to the NH (23% of global ice-free ocean surface area). Usable percent of full power drops to 68% in regions with the fastest ($\overline{U}$ = 16 m s^{-1}), most variable (σ = 6 m s^{-1}). Further, a 58% (43%) gain in mean power is realized within the NH (SH) winter ST region by increasing the cut-out speed from 20 m s^{-1} to 30 m s^{-1}.

[24] NH summer ST winds are slower ($\overline{U}$ = 6–10 m s^{-1}) and steadier (σ = 2–4 m s^{-1}). An exception to this resides over the Labrador Current where winds are still relatively fast ($\overline{U}$> 12 m s^{-1}). Smaller SH circumpolar region interseasonal swings in wind speed statistics are evident when comparing winter and summer curves with those of the NH in Figures 8 and 4. Within the NH summer ST, turbines with cut-out speeds faster than 20 m s^{-1} will harvest little additional power (Figure 8 and Figure 7, right). As the SH ST summer curve in Figure 8 asymptotes to 1020 W m^{-2} at 24 m s^{-1}, a 13% power gain is realized.

[25] Regions characterized with year-round moderate ($\overline{U}$ = 5–9 m s^{-1}) and persistent (σ = 1–4 > m s^{-1}) are typically found equatorward of 30° and account for 50% of global ice-free ocean surface area. Thus, even the slowest cut-out speed amongst the three turbines (20 m s^{-1}) is above the wind PDF upper tail for all seasons and minimal power is gained from faster cut-out speeds (Figure 8). Usable power equatorward of 30° is >96% for all cut-out speeds and seasons (Figure 7).

4.3. Coastal Wind Power

[26] The expansive shallow waters of the continental shelves, coastal lands of previous climates, provide a wide transition zone between land and deep ocean (evident in Figures 9 and 10). Although all inland water bodies equatorward of 70° are included, their contribution to this analysis is relatively small compared to the vast oceans with the exception of the Black and Caspian Seas. There is approximately 250,000 km^2 of water surface area per unit depth from the shore to the 50 m isobath. Surface area per unit depth decreases to 130,000 km^2 m^{-1} between the 50 m and 70 m isobaths. The gradual decline in surface area for depths > 70 m could be a manifestation of the increasing slope of the ocean floor beyond the shelf break (the depth of which varies from 70 m to 400 m (Ocean, in Encyclopedia Britannica Online, http://www.britannica.com, accessed 2009). Surface area per unit depth asymptotes to 20,000 km^2 m^{-1} near 400 m indicative of the continental slope. Surface area with depths < 145 m (the average depth of the continental shelf) is approximately 72% (2.1×10^7 km^2) of <500 m deep (2.9×10^7 km^2) surface area and 5.7% (8.3% for 500 m) of surface area of all depths.

[27] Offshore winds are typically faster and more persistent with respect to onshore and typically increase with distance to shore. Two Danish offshore sites 2 km and 11 km from the shore have 30% and 50%, respectively, faster mean wind speeds than an onshore coastal site [*Pryor and Barthelmie*, 2002]. For ice-free regions between 70°N and 70°S, mean winds increase from 7 m s^{-1} in shallow waters to >9 m s^{-1} for waters deeper than 145 m (not shown). Following the trend in mean winds, 80 m mean wind power increases at a rate of approximately 4 W m^{-2} m^{-1} moving from the shore to a depth of 145 m (Figure 11). Mean 80 m wind power plateaus at 900 W m^{-2}, becoming highly variable for depths deeper than 145 m. The increase in variability for depths > 145 m is a result of the smaller ocean surface area and thus, fewer data points for depths between 145 m and 500 m.

[28] A measure of available wind power proportional to siting area is defined as

$$P_s = (P_w/A_r)\, A_s, \tag{5}$$

where A_s is the ocean surface area. Given this measure, the power produced within a region by a wind farm (P_t) can easily be estimated given the turbine siting density (T_d, number of turbines per km^2), area swept by each turbine's rotors (A_r) and specific turbine efficiency value (C_e, a maximum value of 59.3%)

$$P_t = P_s\, T_d\, A_r\, C_e. \tag{6}$$

This is the maximum power extracted, not taking into consideration other turbine specific mechanical limitations manifested in a turbine power curve.

[29] Technology which allows for deeper water turbine placement provides access to more wind power. Approximately 3.7% of ice-free global ocean 80 m wind power exists in depths < 500 m. As expected, more than half (56%) of this power resides over the relatively massive global continental shelf (<145 m depth, Figure 11). These are conservative estimates given the lack of scatterometer measurements within 30 km of the coast [*Pickett et al.*, 2003]. A steep power per depth rate of 20–45 MW km^2 m^{-2} m^{-1} exists between depths of 20 and 145 m (Figure 12). The cumulative power curve inflection point is consistent with the location of the shelf break (145 m depth) beyond which wind power accumulates at a slower rate until the depths of the abyssal plain. Thus, for waters deeper than 200 m, power per depth is less than 12 MW km^2 m^{-2} m^{-1}.

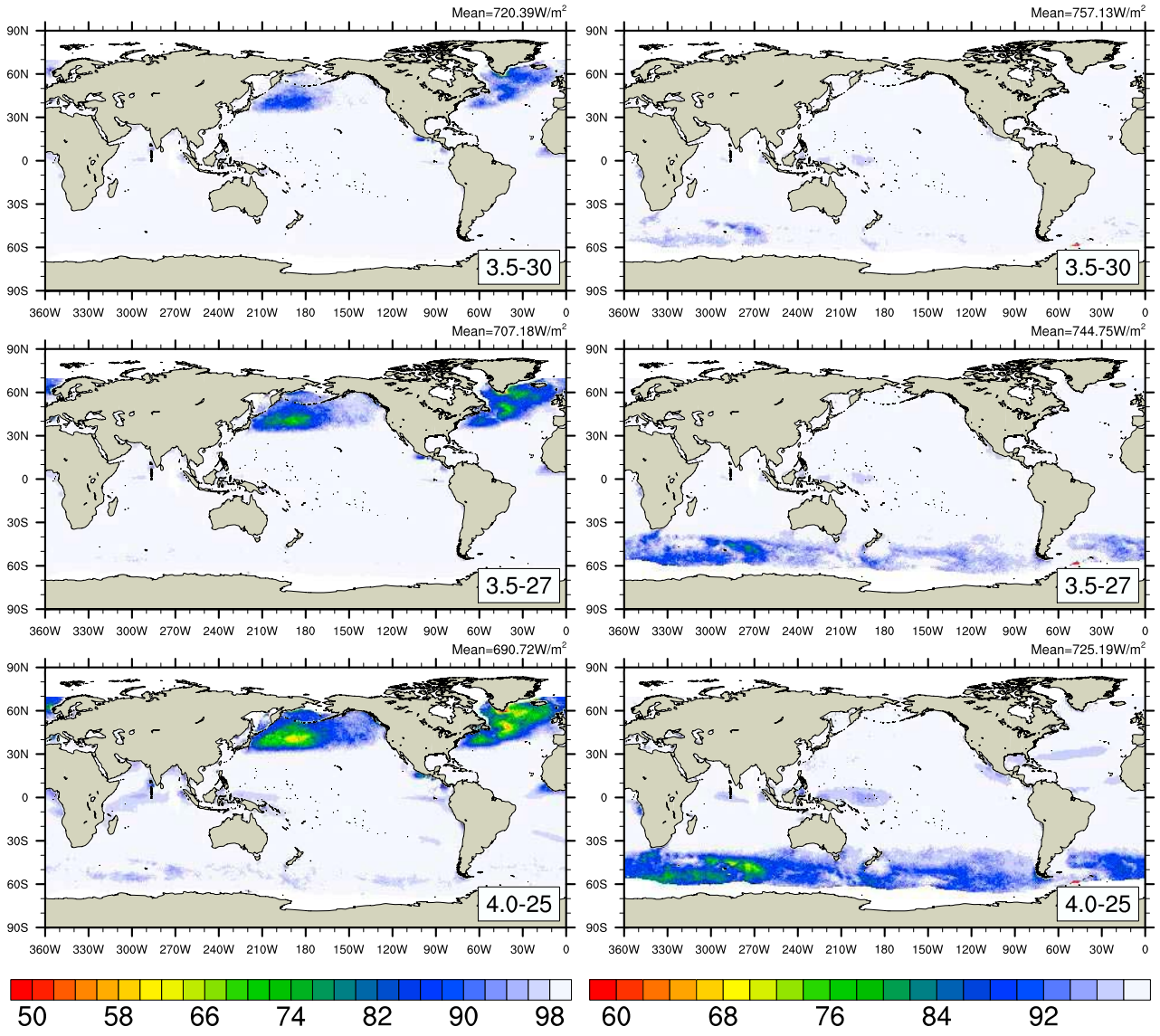

Figure 7. The 2000–2006 (left) DJF and (right) JJA usable percent of full PDF 80 m wind power for three usable wind speed ranges: (top) 3.5–30 m s^{-1}, (middle) 3.5–27.0 m s^{-1}, and (bottom) 4.0–25.0 m s^{-1}.

[30] Plans for wind farm placement in 60 m deep waters are currently underway. Technology which allows wind turbine placement in waters as deep as 200–300 m is currently being refined [*Breton and Moe*, 2009]. Ocean surface area with depths between 60 and 200 m (7.0×10^7 km^2) contains 2.6× the power of depths < 60 m. More importantly, not all of this increase in power is from the addition of siting space. Mean 80 m wind power increases from 500 W m^{-2} to 900 W m^{-2} between 60 m and 200 m depths. However, wind power costs increase with distance to shore, deeper waters and total capacity [*Snyder and Kaiser*, 2009]. Making offshore wind power more cost competitive will require technological advancements, dwindling onshore siting space and larger, more powerful turbines.

5. Discussion

[31] Usable percent of 80 m available wind power is evaluated for three scenarios based on existing, planned and future wind turbine technology. We choose existing technological specifications to include a maximum siting depth of 45 m, a turbine hub height of 50 m and a cut-out speed of 25 m s^{-1}. Planned wind farms have hub heights of typical modern-day offshore wind turbines (80 m, such as those proposed in the Cape Wind Project on Nantucket Sound (http://www.capewind.org/). Planned siting depths are as deep as 60 m [*Breton and Moe*, 2009]. Future wind farms could contain hub heights of 100 m (hub height of next generation turbines [*DOE*, 2008]) and a cut-out speed of 30 m s^{-1} (both of which are within the RE Power 5 and 6M turbine specifications). Next generation wind turbines could be placed in waters as deep as 200 m, which is about a middle target estimate of future floating turbine depths.

[32] The combined impact of wind turbine hub height, cut-out speed and siting depth placement on ice-free global ocean available 80 m wind power is shown in Table 2. Of the three characteristics, depth is the most important, followed by

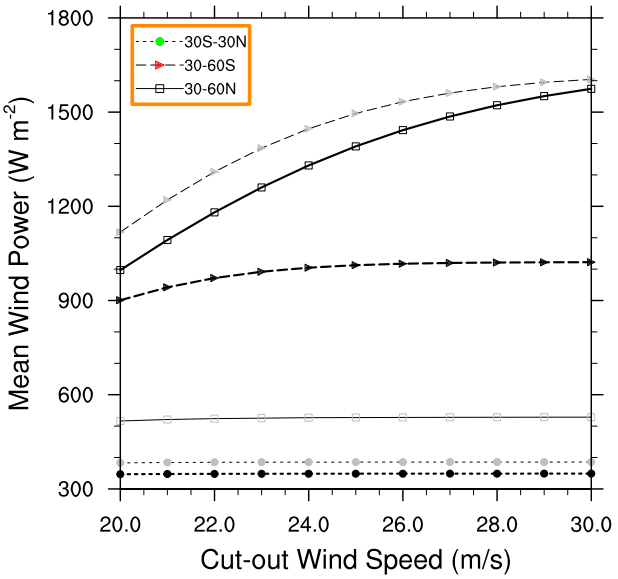

Figure 8. The 2000–2006 DJF (black) and JJA (gray) mean 80 m wind power versus cut-out speed for three latitude bands (30°S–30°N, 30°S–60°S, and 30°N–60°N).

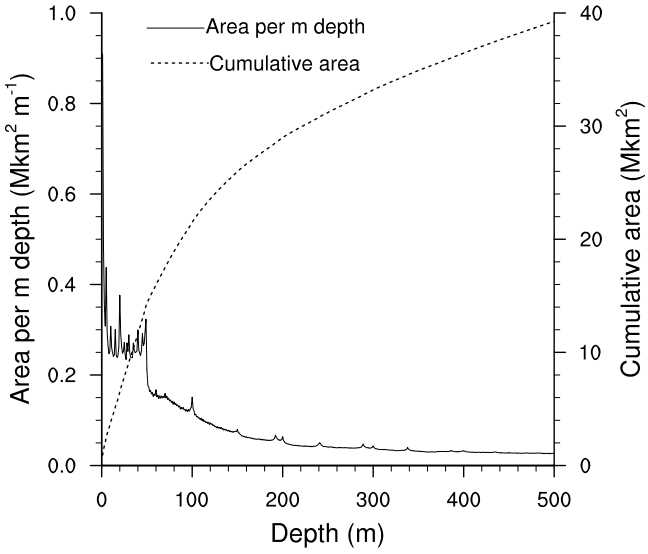

Figure 10. Surface area per unit depth and cumulative surface area down to 500 m depth between 70°N and 70°S (from 1 arc-minute resolution bathymetry data). Total ocean (including large inland bodies of water) surface area between 70°N and 70°S is 3.48×10^8 km^2.

hub height and cut-out speed. The roughly 3% of ocean surface area with depths < 45 m contains 0.40% (50 m hub height) of available 80 m wind power compared to 0.73% and 2.73% for depths less than < 60 m and 200 m, respectively. Global wind power at 50 m is 89% of available 80 m power compared to 106% at 100 m. Finally, usable percent of 80 m global wind power ranges from 87% to 106% for cut-out speeds of 25 m s^{-1} and 30 m s^{-1}, respectively. However, locations where the cut-out speed has a substantial impact on usable power are limited to wintertime remote ocean regions where turbine siting is not anticipated. Thus, cut-out speeds have a small impact on offshore wind power when considering regions with viable siting depths. At 50 m, 0.40% (0.91 GW km^2 m^{-2}) of available 80 m wind power (227.45 GW km^2 m^{-2}) can be harvested, over offshore depths ≤ 45 m and between 4.0 and 25 m s^{-1}. In contrast, 2.73% (6.21 GW km^2 m^{-2}) of available ocean 80 m wind power can be harvested at 100 m, over offshore depths ≤ 200 m and between 3.5 and 30 m s^{-1}.

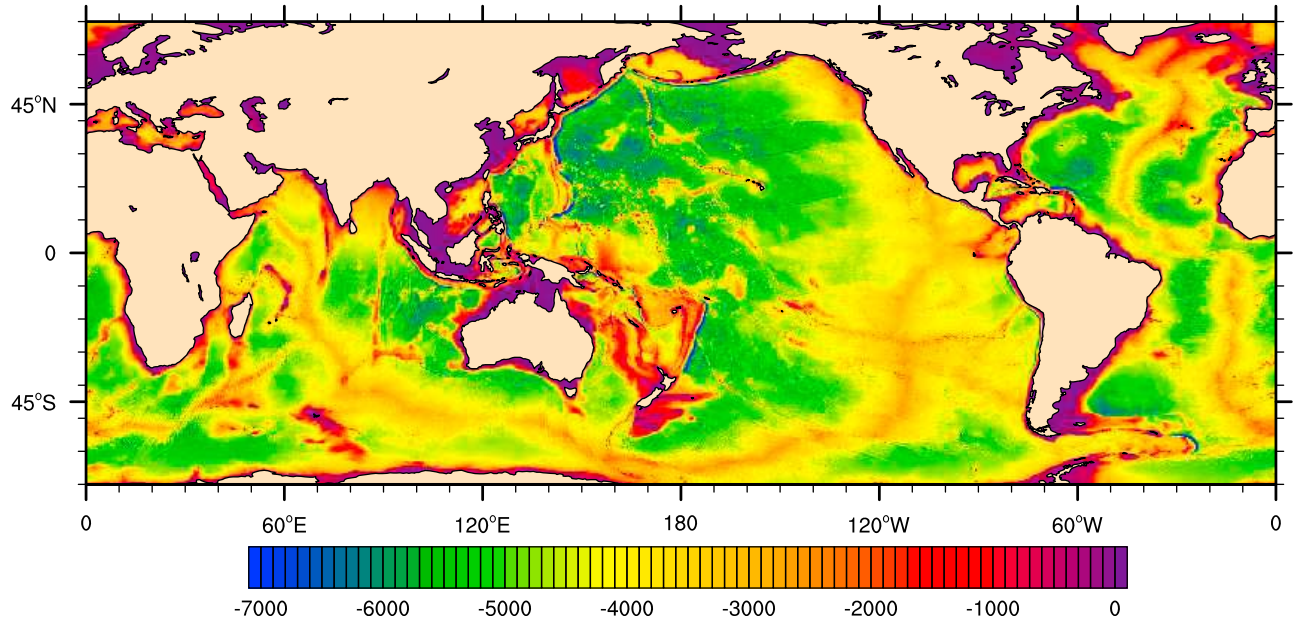

Figure 9. Ocean floor bathymetry between 70°N and 70°S (m, regridded to 0.25° × 0.25° resolution).

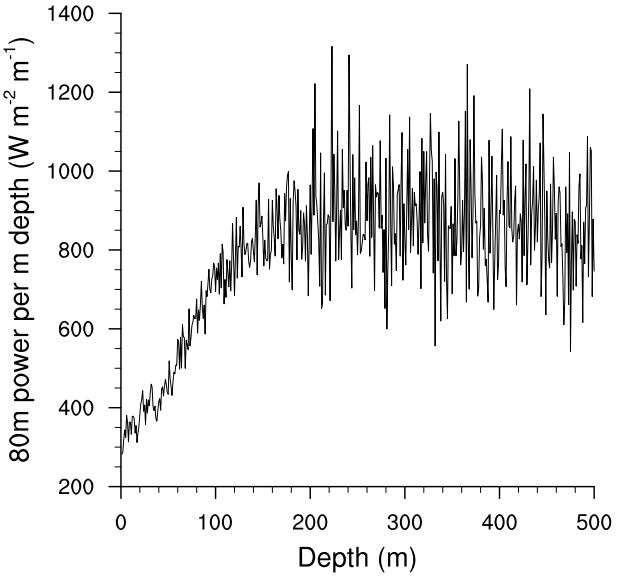

Figure 11. The 2000–2006 average 80 m wind power per unit siting depth.

[33] We now make the transition between available power and power produced by a wind farm. *Archer and Jacobson* [2005] evaluated global onshore 80 m wind power for locations with at least class 3 80 m wind speeds (≥6.9 m s^{-1}). We estimate global offshore wind power using larger (rotor diameters of 90–126 m, hub heights of 80–100 m) and more powerful (3000–5000 kW) turbine specifications compared to onshore (rotor diameter of 77 m and 1500 kW). As much as 59.3% (Betz limit) of available power is theoretically extractable with turbine generator/gearbox inefficiencies further reducing this limit. A wind turbine power curve provides an estimate of the actual power produced by a specific turbine at each wind speed. Wind power at 80 m and 100 m is calculated for class 3 or better sites using three offshore turbine power curves integrated over the wind speed PDF for three siting depth limits (see Tables 3 and 4). Turbine power curves are digitized from the manufacturers' product brochures. Turbine siting density is determined using two turbine spacing expressions ($4D \times 7D$ [*Archer and Jacobson*, 2005] and $10D \times 5D$ [*Manwell et al.*, 2002] where D is the rotor diameter).

[34] As expected, surface area with fast wind speeds (class ≥ 3) increases with depth (Table 3). However, there is less surface area with 100 m class ≥ 3 winds than at 80 m for all depths. Ocean surface area with depths less than 45 m and 200 m with fast mean winds ranges from 8% (1.4 M km^2) to 39% (6.4 M km^2), respectively, of onshore fast wind area (12.7% of 130 M km^2 [*Archer and Jacobson*, 2005]). The only exclusion zone in this study is the coastal band from the shore to 30 km where scatterometer measurements are not available. Depending on location, a narrower exclusion zone (say, to about 10 km) could exist due to visual impacts. Either way, it is important to note that surface area determined here is underestimated.

[35] For the three turbines considered, offshore wind farms consisting of the smallest and least powerful turbines produce the most power. Rated and mean power increase from the smallest to the largest rotor diameter. The best fit curve to the rated power versus rotor diameter relationship for these three turbines is a quadratic function

$$P(D) = 0.57D^2 - 69.12D + 4545.45, \quad (7)$$

where P (kW) is the rated power and D (m) is the rotor diameter. The power produced by a wind farm is proportional to the siting area and power produced by each turbine and inversely proportional to turbine spacing. Wind farm turbine spacing increases with the square of the rotor diameter and is the dominant term in the wind farm power output formula

$$P(D)_t = A_s \frac{P(D)}{\left[\epsilon(0.001D)^2\right]}, \quad (8)$$

where $P(D)_t$ (kW) is wind farm power, ϵ is 28 or 50, and A_s (km^2) is the ocean surface area. Thus, when comparing wind farm power generated using 126 m to that from 90 m rotor diameters, large percent power increases (65%) are dwarfed by larger percent increases in turbine spacing (95%). Increases in capacity factors (from smaller to larger turbines) could help recover some of this decrease in total wind farm power. However, capacity factors were nearly identical among the three turbines for each ocean depth constraint, attributable to less variable near-shore winds. Thus, turbines with 100 m hub heights, 90 m diameter rotors and 3.0 MW rated power placed in wind farms throughout global, ice-free waters no deeper than 200 m and not visible from the coast could generate as much as 39 TW or 54% of total onshore power.

6. Conclusions

[36] We extend the work of *Capps and Zender* [2009], evaluating available global ocean wind power at multiple heights, usable speed ranges and siting depths. Available

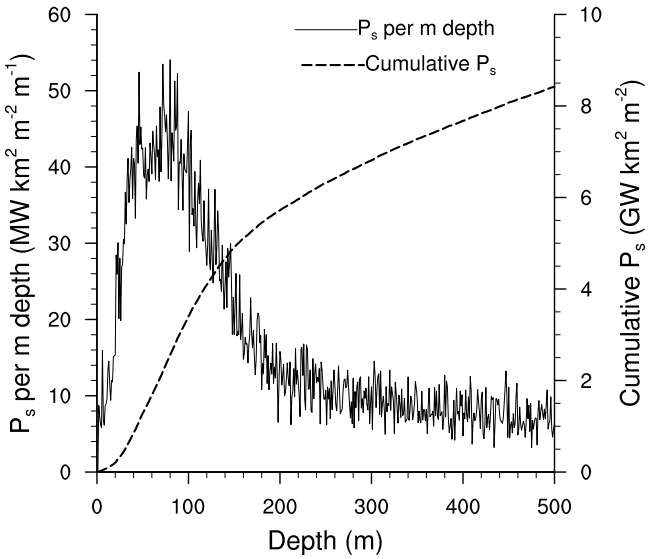

Figure 12. The 80 m power × surface area (P_s) per unit siting depth and cumulative P_s (ocean bathymetry regridded to 0.25° × 0.25° resolution).

Table 2. The 2000–2006 Ocean Usable Wind Power Compared to 80 m Available Wind Power Based on Existing, Planned, and Future Scenarios of Wind Turbine Hub Height, Usable Speeds, and Siting Depth

	Existing	Percent Existing Power[a]	Planned	Percent Planned Power[a]	Future	Percent Future Power[a]
Hub Height	50 m	89%	80 m	100%	100 m	106%
Usable Speeds	4–25 m s^{-1}	87%	3.5–27 m s^{-1}	98%	3.5–30 m s^{-1}	106%
Siting Depth	≤45 m	0.40%	≤60 m	0.74%	≤200 m	2.75%
Combined		0.40%[b]		0.73%[c]		2.73%[d]

[a]Percent of 2000–2006 80 m available ocean wind power (227.45 GW km^2 m^{-2}).
[b]Usable wind power of 0.91 GW km^2 m^{-2}.
[c]Usable wind power of 1.66 GW km^2 m^{-2}.
[d]Usable wind power of 6.21 GW km^2 m^{-2}.

global ocean wind power is evaluated for several heights between 10 m and 100 m. Usable percent of available power, dependent upon turbine cut-in and cut-out speeds, is estimated for three multimegawatt offshore turbines. Next, we estimate the power accessible to current seabed resting and envisioned floating offshore wind turbines. Finally, global offshore wind power is estimated using three wind turbine power curves, three ocean depth limits and two wind farm siting densities. Beyond the scope of this study, usable power is also dependent upon wind turbine downtime due to maintenance and repair and turbine generator and gearbox inefficiencies.

[37] The sensitivity of wind power to height is evaluated over the ice-free global oceans for 2000–2006. Global mean 100 m 2000–2006 wind power (776 W m^{-2}) is 1.6 times 10 m (487 W m^{-2}). Due to increased wind shear and the cubic dependence of wind power on speed, frequent high wind speed regions have the greatest increase in power with height. Thus, the storm track regions experience the greatest increase in annual mean wind power with height. During 2000–2006, a 100 m hub height wind turbine could capture 69% (74%) more power within the Northern (Southern) Hemisphere storm track than at 10 m. Slower winds with nearly logarithmic profiles within the tropics result in an average power gain of 30%. Rates of increases within the Northern Hemisphere NH storm track are highly seasonal, ranging from 4–8 W m^{-2} m^{-1} (JJA) to 7–11 W m^{-2} m^{-1} (DJF). Maximum power increases with height are found over the Labrador current during summer and the Southern Hemisphere SH storm track region throughout all seasons.

[38] We truncated wind power density calculated from fitted Weibull distributions between the cut-in and cut-out speeds of three modern offshore wind turbines. Usable power percent of full power declines as winds become faster and more variable. Over approximately 11% of the NH wintertime ice-free global oceans, a turbine with a cut-out speed of 25 m s^{-1} harvests between 55 and 85% of available power.

Table 3. Ocean Surface Area and Mean Wind Speed for Class ≥3 Regions and Depths ≤45, 60, and 200 m at 80 m and 100 m Heights[a]

Case	Depth (m)	A_{s80} (Mkm^2)	$\overline{U}_{80}$ (m s^{-1})	A_{s100} (Mkm^2)	$\overline{U}_{100}$ (m s^{-1})
1	45	1.40	8.23	1.32	8.49
2	60	2.19	8.36	2.06	8.64
3	200	6.47	9.10	6.25	9.43

[a]Class ≥ 3 regions are ≥ 6.9 m s^{-1} (80 m) and ≥ 7.1 m s^{-1} (100 m). A_s, ocean surface area; $\overline{U}$, mean wind speed.

Within the wintertime NH storm track, a 2–3 m s^{-1} change in turbine cut-out speed can result in a 5–7% change in usable power. For most regions, summertime usable power is greater than 95% of available power for cut-out speeds faster than 24 m s^{-1}. Also, summertime regions experience a minimal power gain from cut-out speeds faster than 20 m s^{-1}, with year-round minimal gains within the tropics.

[39] Plans for wind farm placement in 60 m deep waters are currently underway. Technological innovations and learning will likely continue to allow placement of turbines in waters as deep as the shelf break (~145 m). More than half of the wind power over siting depths less than 500 m resides over the massive continental shelf. The added benefit from moving into deeper waters is maximized for depths above the shelf break. Per meter depth increase, mean wind power and total available wind power increase by 4 W m^{-2} and 20–45 MW km^2 m^{-2}, respectively, from the shore to the shelf break. Reduced horizontal ocean surface area over the steep continental slope and a zero trend in mean wind speeds with depth results in a reduced rate of return on investment (<12 MW km^2} m^{-2} m^{-1}). Further technological developments will provide larger, more powerful turbines with siting in deeper waters harnessing faster offshore winds. However, it is likely that costs will always increase for deeper, more remote waters. Thus, only until after the wind resources of continental shelves are exploited will resources over waters deeper than the shelf break be explored. In the meantime, ship-based platforms harnessing winds for marine vessel power and/or climate mitigation efforts are possible consumers of such deep water wind resources [*Salter et al.*, 2008].

[40] We assess the combined impact of hub height, cut-out speed and siting depth upon ice-free global ocean 80 m available power. At three heights, we truncate the power density curve between three usable speed ranges. Usable wind power multiplied by the occupied surface area is integrated over the ocean surface with siting depth limits consistent with existing, planned and future wind farms. As much as 0.40% of available 80 m wind power is available to existing technology while wind farms of the future could be exposed to as much as 2.73% of 80 m available wind power.

[41] Global offshore wind power production is estimated using power curves of three turbines within three ocean isobaths for regions with class 3 or faster wind speeds. There is an optimal blend of siting density and individual turbine power and efficiency which maximizes wind farm power production for a given surface area. This study assumes global homogeneous offshore wind farms within which all turbines are one of the three evaluated here. In reality, the

Table 4. Total Wind Power Potential for Locations Characterized With Class 3 Wind Speeds or Faster, Three Turbines, and Ocean Depths ≤45, ≤60, and ≤200 m

	D[a]	T_{d1}[b]	T_{d2}[c]	Case[d]	CF_{80}[e]	P_{t80}[f]	P_{t80}[g]	CF_{100}[h]	P_{t100}[i]	P_{t100}[j]
VestasV90 3.0MW	90	2.47	4.41	1	0.38	3.96	7.07	0.41	3.98	7.11
				2	0.40	6.40	11.44	0.42	6.40	11.42
				3	0.46	21.95	39.20	0.48	22.29	39.80
GE 3.6MW	104	1.85	3.30	1	0.39	3.65	6.52	0.41	3.63	6.48
				2	0.40	5.83	10.42	0.42	5.82	10.40
				3	0.46	19.95	35.62	0.49	20.24	36.14
RE Power 5MW	126	1.26	2.25	1	0.38	3.39	6.05	0.41	3.39	6.06
				2	0.40	5.45	9.73	0.42	5.46	9.75
				3	0.46	18.79	33.55	0.49	19.13	34.16

[a]Rotor Diameter (m).
[b]Siting density (km^{-2}) using $10D \times 5D$.
[c]Siting density (km^{-2}) using turbine spacing $4D \times 7D$.
[d]Ocean depth cases (see Table 3).
[e]The 80 m capacity factor.
[f]Total 80 m wind power potential (TW) for a turbine spacing $10D \times 5D$.
[g]Total 80 m wind power potential (TW) for a turbine spacing $4D \times 7D$.
[h]The 100 m capacity factor.
[i]Total 100 m wind power potential (TW) for turbine spacing $10D \times 5D$.
[j]Total 100 m wind power potential (TW) for turbine spacing $4D \times 7D$.

turbine placed within each wind farm or at each location is the turbine which has the highest capacity factor given the local wind speed statistics. Nonetheless, of the three turbines considered in this study, offshore wind farms populated with the smallest, least powerful turbine produce the most amount of power, as much as 54% of total onshore power.

[42] **Acknowledgments.** Level 3 QuikSCAT data were obtained from NASA's Jet Propulsion Laboratory (http://podaac.jpl.nasa.gov). Woods Hole Oceanographic Institution third version of global ocean-surface heat flux product was obtained from http://oaflux.whoi.edu/. Henry Butowsky supported our data analysis by improving the freely available netCDF operators (NCO, http://nco.sourceforge.net/). This work supported by NSF IIS-0431203, ARC-0714088, and NASA NNX07AR23G.

References

Amante, C., and B. W. Eakins (2008), ETOP01 1 arc-minute global relief model: Procedures, data sources and analysis, report, NESDIS, NOAA, U.S. Dep. of Comm., Silver Spring, Md.

American Wind Energy Association (2009), American Wind Energy Association annual wind industry report: Year ending 2008, Washington, D. C.

Archer, C. L., and M. Z. Jacobson (2005), Evaluation of global wind power, *J. Geophys. Res.*, *110*, D12110, doi:10.1029/2004JD005462.

Arya, S. P. (2001), *Introduction to Micrometeorology*, 2nd ed., Academic, San Diego, Calif.

Betz, A. (1920), Das maximum der theoretisch möglichen ausnützung des windes durch windmotoren, *Z. Gesamte Turbinenw.*, *26*, 307–309.

Breton, S.-P., and G. Moe (2009), Status, plans and technologies for offshore wind turbines in Europe and North America, *Renewable Energy*, *34*, 646–654.

Capps, S. B., and C. S. Zender (2008), Observed and CAM3 GCM sea surface wind speed distributions: Characterization, comparison, and bias reduction, *J. Clim.*, *21*, 6569–6585.

Capps, S. B., and C. S. Zender (2009), Global ocean wind power sensitivity to surface layer stability, *Geophys. Res. Lett.*, *36*, L09801, doi:10.1029/2008GL037063.

Chelton, D. B., and M. H. Freilich (2005), Scatterometer-based assessment of 10-m wind analyses from the operational ECMWF and NCEP numerical weather prediction models, *Mon. Weather Rev.*, *133*, 409–429.

Department of Energy (DOE) (2008), 20% wind energy by 2030, report, Washington, D. C.

Fairall, C. W., E. F. Bradley, J. E. Hare, A. A. Grachev, and J. B. Edson (2003), Bulk parameterization of air-sea fluxes: Updates and verification for the COARE algorithm, *J. Clim.*, *16*, 571–591.

Hoffman, R. N., and S. M. Leidner (2005), An introduction to the near-real-time QuikSCAT data, *Weather Forecasting*, *20*, 476–493.

Jacobson, M. Z. (2009), Review of solutions to global warming, air pollution, and energy security, *Energy Environ. Sci.*, *2*, 148–173.

Kanamitsu, M., W. Ebisuzaki, J. Woollen, S.-K. Yang, J. J. Hnilo, M. Fiorino, and G. L. Potter (2002), NCEP–DOE AMIP-II reanalysis (r-2), *Bull. Am. Meteorol. Soc.*, *83*, 1631–1643.

Kelly, K. A., S. Dickinson, M. J. McPhaden, and G. C. Johnson (2001), Ocean currents evident in satellite wind data, *Geophys. Res. Lett.*, *28*, 2469–2472.

Kempton, W., C. Archer, A. Dhanju, and R. W. Garvine (2007), Large CO_2 reductions via offshore wind power matched to inherent storage in energy end-uses, *Geophys. Res. Lett.*, *34*, L02817, doi:10.1029/2006GL028016.

Lange, B., S. Larsen, J. Hojstrup, and R. Barthelmie (2004), Importance of thermal effects and sea surface roughness for offshore wind resource assessment, *J. Wind Eng. Ind. Aerodyn.*, *92*, 959–988.

Lange, M., and U. Focken (2005), *Physical Approach to Short-Term Wind Power Prediction*, 1st ed., Springer, Oldenburg, Germany.

Liu, W. T. (2002), Progress in scatterometry application, *J. Oceanogr.*, *58*, 121–136.

Liu, W. T., W. Tang, and X. Xie (2008), Wind power distribution over the ocean, *Geophys. Res. Lett.*, *35*, L13808, doi:10.1029/2008GL034172.

Lu, L., H. Yang, and J. Burnett (2002), Investigation on wind power potential on Hong Kong islands—An analysis of wind power and wind turbine characteristics, *Renewable Energy*, *27*, 1–12.

Manwell, J., J. McGowan, and A. Rogers (2002), *Wind Energy Explained: Theory, Design and Application*, John Wiley, West Sussex, U. K.

Martinez, E., F. Sanz, S. Pellegrini, E. Jimenez, and J. Blanco (2009), Life cycle assessment of a multi-megawatt wind turbine, *Renewable Energy*, *34*, 667–673.

Matthews, J. N. A. (2009), Superconductors to boost wind power, *Phys. Today*, *62*, 25–26.

Mears, C. A., D. K. Smith, and F. J. Wentz (2001), Comparison of special sensor microwave imager and buoy-measured wind speeds from 1987 to 1997, *J. Geophys. Res.*, *106*, 719–729.

Medeiros, B., A. Hall, and B. Stevens (2004), What controls the mean depth of the PBL, *J. Clim.*, *18*, 3157–3172.

Monahan, A. H. (2006), The probability distribution of sea surface wind speeds. Part I: Theory and seawinds observations, *J. Clim.*, *19*, 497–520.

Pickett, M. H., W. Tang, L. K. Rosenfeld, and C. H. Wash (2003), QuikSCAT satellite comparisons with nearshore buoy wind data off the U.S. west coast, *J. Atmos. Oceanic Technol.*, *20*, 1869–1879.

Pimenta, F., W. Kempton, and R. Garvine (2008), Combining meteorological stations and satellite data to evaluate the offshore wind power resource of southeastern Brazil, *Renewable Energy*, *33*, 2375–2387.

Pryor, S. C., and R. J. Barthelmie (2002), Statistical analysis of flow characteristics in the coastal zone, *J. Wind Eng. Ind. Aerodyn.*, *90*, 201–221.

Salter, S., G. Sortino, and J. Latham (2008), Sea-going hardware for the cloud albedo method of reversing global warming, *Philos. Trans. R. Soc. A.*, *366*, 3989–4006.

Sampe, T., and S.-P. Xie (2007), Mapping high sea winds from space, *Bull. Am. Meteorol. Soc.*, *88*, 1965–1978.

Serpetzoglou, E., B. A. Albrecht, P. Kollias, and C. W. Fairall (2008), Boundary layer, cloud, and drizzle variability in the southeast Pacific stratocumulus regime, *J. Clim.*, *21*, 6191–6214.

Snyder, B., and M. J. Kaiser (2009), Ecological and economic cost-benefit analysis of offshore wind energy, *Renewable Energy*, *34*, 1567–1578.

Yu, L., X. Jin, and R. A. Weller (2008), Multidecade global flux datasets from the objectively analyzed air-sea fluxes (OAFlux) project: Latent and sensible heat fluxes, ocean evaporation, and related surface meteorological variables, *OAFlux Tech. Rep. OA-2008-01*, 64 pp., WHOI, Woods Hole, Mass.

S. B. Capps and C. S. Zender, Department of Earth System Science, University of California, Irvine, CA 92697, USA. (scapps@uci.edu; zender@uci.edu)